Experimental Study of Heat Transfer on the Internal Surfaces of a Double-Wall Structure with Pin Fin Array

Wei Zhang [1,2,*], Huiren Zhu [1] and Guangchao Li [2]

[1] School of Power and Energy, Northwestern Polytechnical University, Xi'an 710072, China; zhuhr@nwpu.edu.cn

[2] School of Aero-Engine, Shenyang Aerospace University, Shenyang 110136, China; ligc706@163.com

[*] Correspondence: emma7691@163.com; Tel.: +86-24-89728918

check for updates

Abstract: The double-wall structure is one of the most effective cooling techniques used in many engineering applications, such as turbine vane/blade, heat exchangers, etc. Heat transfer on the internal surfaces of a double-wall structure was studied at impinging Reynolds numbers ranging from 1×10^4 to 6×10^4 using the transient thermochromic liquid crystal (TLC) technique. The two-dimensional distributions of Nusselt numbers and their averaged values were obtained on the impingement surface, target surface and the pin fin surface. The Nusselt number correlations on the surfaces mentioned above were determined as a function of Reynolds number. The results show that the second peak values of the Nusselt number distribution appear on the target surface at all Reynolds numbers studied in this paper for a short distance of the target surface to impingement surface. This phenomenon becomes significant with the further increase of the Reynolds number. The difference between the Nusselt number at the second peak and the stagnation point decreases with the increasing Reynolds number. The maximal Nusselt number regions on the impingement surface appear at the left and right sides of the pin fins between the two impingement holes. The Nusselt numbers of the pin fin surfaces are highly dependent on their various locations in the double-wall structures. The contributions of the impingement surface, pin fin surface and target surface to the overall heat transfer rate are analyzed. The target surface contributed the largest amount of heat transfer rate with a value of about 62%. The heat transfer contribution is from 18% to 21% for the impingement surface and 16% to 18% for the pin fin surfaces within the studied Reynolds numbers.

Keywords: gas turbine; jet impingement; double-wall structure; full-surface temperature measurement; correction of heat transfer coefficient; heat transfer analysis

1. Introduction

In order to increase the propulsion thrust and the thermal efficiency of the advanced gas turbine, the turbine inlet temperature was continuously increased and has been higher than the melting point of the turbine material. Therefore, an effective cooling technique is required to ensure the normal work of the engine. The double-wall structure combined with internal jet impingement [1,2], pin fins [3–5] and the external film cooling [6–8] is one of the most effective cooling techniques used in many engineering applications, such as turbine vane/blade, power electronics, heat exchangers, etc. [9].

The cooling performance is a key parameter on cooling structures. The convection cooling in the holes and film cooling was the dominant factors affecting the overall effectiveness [10]. However, when the hole spacing was sufficiently wide, the through-hole convection was not dominant [11]. Mensch et al. [12] examined the overall effectiveness of a blade endwall with jet impingement and film

cooling; it was found that when only film cooling was used, the cooling effectiveness was high around the film-cooling holes due to convective cooling in the holes. Internal impingement cooling provided more uniform cooling performance than film cooling, and the performance improved markedly with an increase in the blowing ratio. Williams et al. [13] investigated the sensitivity of the overall cooling effectiveness of film cooling and internal cooling on a turbine vane suction side. It was found that the adiabatic film effectiveness decreased when high momentum flux ratios were used for film cooling due to coolant jet separation. The overall cooling effectiveness increased at higher momentum flux ratios due to the increased internal cooling effects.

The microstructures on the plate enhanced the impingement heat transfer and improved the heat transfer uniformity with a negligible pressure loss increase compared with the impingement onto the flat plate [14–16]. The various microroughness, such as the dimple, rib and pin fin, were found to take a different role in the internal heat transfer enhancement of the double-wall. Vinze et al. [17] found that the flat plate was more efficient than a dimpled surface for the jet orifice and dimple pitches of a three-nozzle diameter. The effect of the ribs was to change the influence on the impingement heat transfer in the crossflow [18]. The presence of the rib made the impingement heat transfer rate more uniform in the crossflow [19] and was more useful for low-speed impinging jets [20]. Xu et al. [21] studied the effects of the pin fin arrangement on the heat transfer characteristics in a convergent channel with impingement to obtain the optimal pin fin array. The experiments showed that effusion holes on the pin fin target plates obviously reduced the crossflow in the impingement channel, which improved and uniformed the heat transfer on the endwall of the target plates [22]. Liu et al. [23] found that the grooves underneath the jet holes hindered the impingement flow, and the jet impingement heat transfer was reduced. The vortex–generator pair with a common flow-up configuration promoted the jet penetration in the crossflow and greatly increased the impingement heat transfer on the target wall compared with the baseline case without the vortex–generator pair [24].

The jet configurations and parameters have been investigated in terms of both heat transfer and fluid flow. Singh et al. [25] studied the effect of the nozzle shape on jet impingement heat transfer from a circular cylinder. It was found that the distributions of the Nusselt number in the chordwise direction on a variable-curvature concave surface played an important role in thermal analysis [26]. Pachpute et al. [27] studied the effect of the jet number emerging from round nozzles on the impingement heat transfer from a heated cylinder. They found that the round jet number required for the uniform cooling increased as the curvature ratio increased. Ansu et al. [28] studied the inlet condition on the jet impingement heat transfer using liquid crystal thermography and developed correlations for the Nusselt number as a function of the Reynolds number and separation distance. A smaller separation distance and less crossflow resulted in a better heat transfer performance. A larger separation distance and less crossflow resulted in a smaller pressure loss [29].

As stated above, the pin fin was found to play an important role in the internal heat transfer enhancement of the double-wall structure. However, most of the studies were focused on the heat transfer performance of the target surface with pin fins rather than the pin fins themselves. At the same time, the contribution of heat transfer on the impingement surface to the internal heat transfer could not be ignored. Therefore, it is extremely important to understand the heat transfer characteristics of each surface for the accurate design of the comprehensive cooling of the double-wall structure. In this study, the detailed distributions of the Nusselt numbers of the target surface, impingement surface and pin fin surfaces at the various locations of the double-wall structure were studied using a thermochromic liquid crystal technique. The emphasis of this paper was to analyze the heat transfer contributions of the impingement surface, pin fin surface and target surface to the overall heat transfer rate. The heat transfer characteristics of the pin fins at different locations were also studied in detail. The correlations of the averaged values on the corresponding surfaces were determined as a function of the Reynolds number.

2. Experiment Setup and Procedures

2.1. Test Rigs

The schematics of the test system for the heat transfer of the double-wall structure is shown in Figure 1. The air was supplied by a centrifugal air blower, which can provide a maximum outlet pressure of 0.02 MPa and a maximum mass flow rate of 3000 m^3/h. The air was first fed into the air tank to stabilize it before going through the inlet valve. An orifice plate flowmeter was installed upstream of the air heater to adjust the air mass flow rate. The heater had a rated power of 4 kW, and the highest allowable temperature of the air was 200 °C. An electromagnetic valve was used to control the flow direction of the air. The air was released into the atmospheric environment through an outlet of the electromagnetic valve. After reaching the specified temperature, the air flowed into the double-wall structure rig through another outlet of the electromagnetic valve. Concurrently, the K-type thermocouples placed at an impingement hole inlet and the film hole outlet began to measure the temperature of the air, and the three charge-coupled device (CCD) cameras (Sony HDR-XR; Sony Corp., Tokyo, Japan) also started to capture the images of the thermochromic liquid crystal (TLC) on the tested surfaces at the rate of 25 frames per second. The thermocouple readings were recorded by a temperature data acquisition system (PSI9000 9046 self-compensation acquisition module, 16 channels) and displayed on the computer. The mass flow rate of air entering into impingement holes was determined by the impingement hole jet Reynolds number. As the flow inside the double-wall structure was influenced by the jet impingement and flow across the pin fins together, it was difficult to accurately get the internal velocity magnitude. Therefore, the jet velocity and the diameter of the impingement hole was chosen when defining the Reynolds number. The corresponding Reynolds numbers of 1×10^4 to 6×10^4 were considered. The corresponding images of the test rigs are shown in Figure 2.
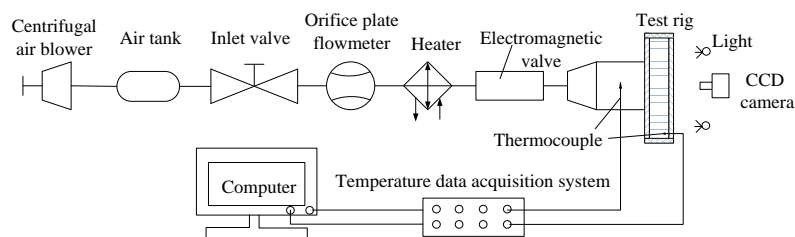
Figure 1. Diagram of the test system. CCD: charge-coupled device.

(**a**)　　　　　　　　　　　　　　　　　　　　　(**b**)

Figure 2. Images of test rigs. (**a**) Test rig of the pin fins. (**b**) Test rig of the target surface.

2.2. Test Configurations

The configurations of the tested rig are shown in Figure 3. It consisted of an impingement plate with three impingement holes of 30-mm diameters, a target plate with 2 rows of staggered film holes installed on both sides and 5 rows of staggered arranged pin fins. The square target plate and the

impingement plate had a thickness of 24 mm and 18 mm, respectively. The arrangements of the pin fin array with S_X/D = 2.5 and S_Y/D = 2.5 were considered. The detailed geometrical parameters of the tested rig are listed in Table 1. Five typical pin fins were marked as A, B, C, D and E. The pin fin C and the impingement holes were in the same row. The dashed lines were center-to-center lines of the impingement holes and of five typical pin fins. The intersections of the lines and pin fin surfaces were defined as leading edges. The pin fins were designated as the first, the second, the third, the fourth and the fifth pin fin rows from the left to right side of the plate. The part of the pin fin near the target plate was designated as the top, and the opposite part was designated as the bottom.
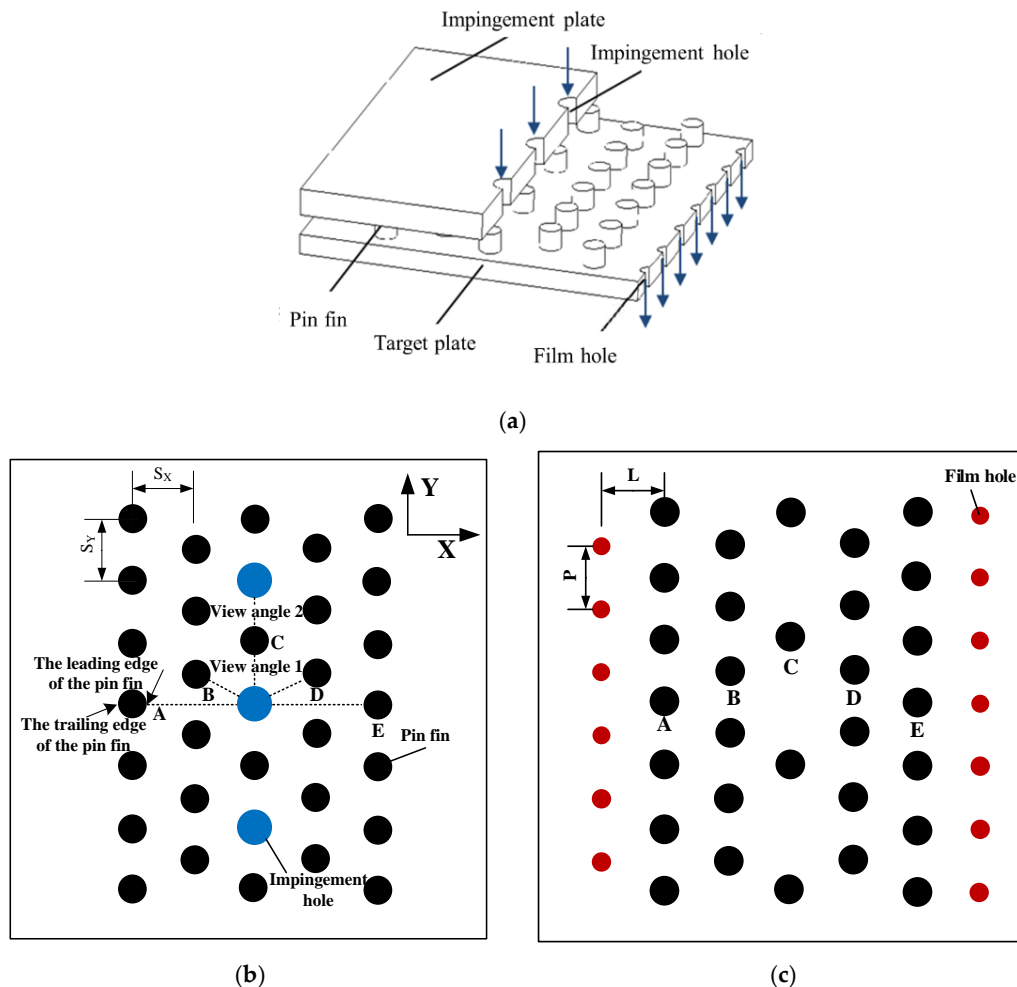
Figure 3. Structures of the tested rig. (**a**) Double-wall structure. (**b**) Impingement plate. (**c**) Target plate.

Table 1. Geometric parameters of the test rig.

D(mm)	D_f/D	D_{Pf}/D	H_{Ip}/D	H_{Pf}/D	H_{Tp}/D	S_X/D	S_Y/D	L/D	P/D
30	0.5	0.8	0.6	0.6	0.8	4	4	4	4

2.3. Test Procedure and Data Reduction

The target surface, impingement surface and pin fin surface were painted with thermochromic liquid crystal (SPN/R30C1W; LCR Hallcrest Co., Glenview, IL, USA) to measure the surface temperature. A thin layer of the black paint was also sprayed on the surfaces for a better display of the color. The sprayed sequence of the black paint and TLC on the surfaces are shown in Figure 4. When measuring the heat transfer coefficients on the impingement surface, the black paint was sprayed on the surface, and then, the TLC was sprayed, since the camera shot on the impingement surface through the target

wall. When measuring the heat transfer coefficients on the target surface, the TLC was sprayed first and, then, the black paint, since the camera shot directly on the surface. The sprayed order of the TLC and the black paint on the pin fins was the same as that on the impingement surface. The calibration of the TLC was performed to determine the relationship between the temperature and the hue and saturation value before the heat transfer experiment. The shooting views have little effect on the calibration curves, and the maximal temperature difference was less than 0.2 K when the view angles were less than 60°, as shown in Figure 5. The temperature of the surface was obtained by the hue–temperature curve. The experiment was performed in a laboratory, which was in a dark enclosure to prevent interference from the surrounding light noise. White LED lights were used in the experiment process.
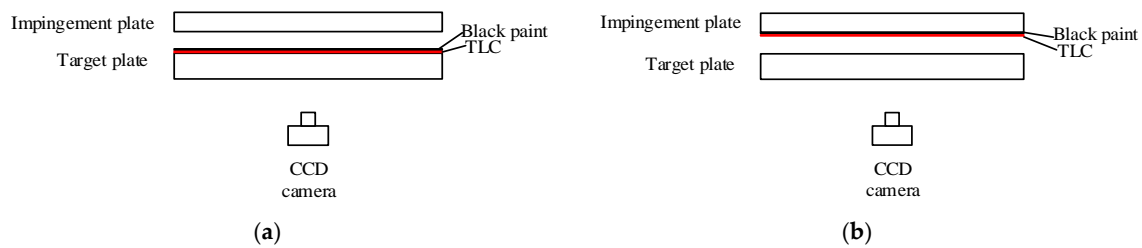
Figure 4. The sprayed sequence of the black paint and thermochromic liquid crystal (TLC). (**a**) Target surface. (**b**) Impingement surface.
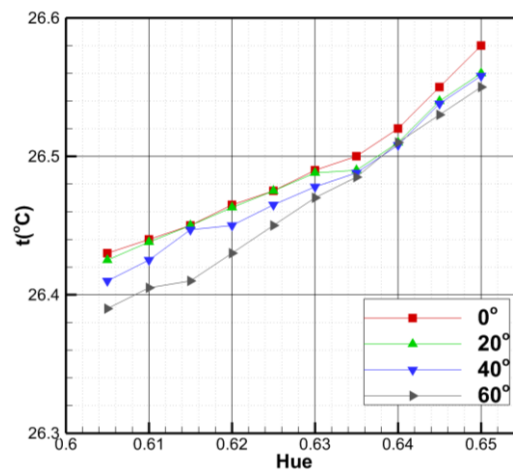
Figure 5. Calibration curves of the TLC.

The theory on the thermochromic liquid crystal technique for heat transfer measurements can be found in the literature [30,31]. The change of the wall temperature can be described by a one-dimensional semi-infinite transient unsteady heat conduction equation. Plexiglas with low thermal diffusivity (0.105×10^{-6} m^2/s) is well-suited for the heat transfer coefficient measurements using the transient conduction model. Based on the square target plate thickness of 24 mm, the process of the transient heat transfer test must be completed in 3 min so that the thermal disturbance of the tested surface does not transfer to the back surface of the test plate with an error of 0.5% by a semi-infinite heat conduction analysis on the flat plate. By solving the equation with the initial and boundary conditions, the nondimensional temperature and the local heat transfer coefficient can be obtained by the following equation:

$$\frac{T_w - T_0}{T_c - T_0} = 1 - \exp\left(\frac{h^2\tau}{\rho_w c_w \lambda_w}\right) erfc\left(\frac{h\sqrt{\tau}}{(\rho_w c_w \lambda_w)^{1/2}}\right) \tag{1}$$

Since the coolant (air) temperature is a function of time, the final equation of the heat transfer coefficient is represented as follows:

$$T_{\mathrm{w}}(\tau) = T_0 + \sum_{i=1}^{n} (T_{c_i} - T_{c_{i-1}})U(\tau - i) \times \left[1 - \exp\left(\frac{h^2}{\rho_w c_w \lambda_w}(\tau - i)\right)erfc\left(\frac{h}{\sqrt{\rho_w c_w \lambda_w}} \sqrt{\tau - \tau_i}\right)\right] \tag{2}$$

where $U(\tau - i)$ is the step function.

As two thermocouples measuring the coolant temperature were located at the impingement hole inlet and film hole outlet, the local temperatures of the coolant inside the double-wall structure could been interpolated in the X direction.

When measuring heat transfer coefficients on the surfaces of the pin fins, which were not flat plates, the correction of the solving equation was carried out, and the detailed method can refer to the literature [32].

Based on the jet hole diameter and jet mean velocity at the entrance, the Reynolds number was defined as:

$$Re = \rho V D / \mu \tag{3}$$

The Nusselt number was given by:

$$Nu = hD/\lambda_c \tag{4}$$

where h was the heat transfer coefficient calculated by Equation (2), and λ_c was the thermal conductivity of the coolant air.

The spanwise averaged Nusselt number and surface averaged Nusselt number can been obtained by Equations (5) and (6):

$$Nu_{\mathrm{ave}} = \frac{1}{n}\sum_{j=1}^{n} Nu_j \tag{5}$$

$$Nu_{\mathrm{ave-s}} = \frac{1}{m \times n}\sum_{k=1}^{m}\sum_{j=1}^{n} Nu_{kj} \tag{6}$$

2.4. Uncertainty Analysis

The uncertainty analysis was performed using the method proposed by Abernethy et al. [33]. The overall uncertainty of the Nusselt number was dependent on the color change time, the temperature and the local heat transfer coefficient. The individual uncertainty in the measurement of the color change time was 0.04 s, which was the time interval of two frames based on the sampling frequency of 25 frames per second by camera. The uncertainties of the coolant temperature and initial surface temperature measured by the calibrated K-type thermocouples were 0.2 K. The uncertainty of the tested surface temperature measured by TLC was 0.4 K, because the TLC was calibrated by thermocouples. The overall uncertainty of the Nusselt number at $Re = 6 \times 10^4$ was shown in Figure 6, which had variable values at different positions on the target and impingement surfaces, respectively. The maximal uncertainty was 15% on a stagnation region of the target surface and was 22% near the impingement hole of the impingement surface. The uncertainty of the heat transfer coefficient caused by lateral heat conduction was less than 3.5% [34].

(a)   (b)
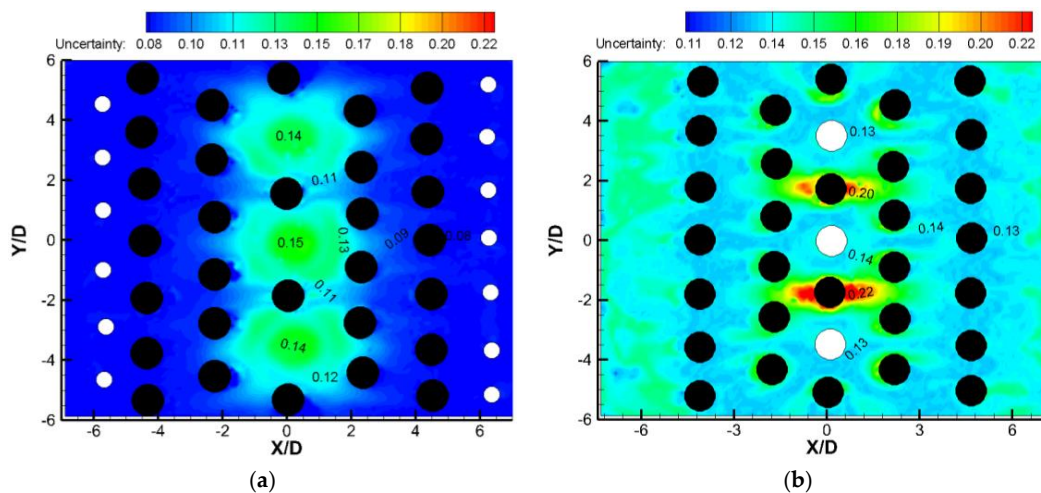
Figure 6. Uncertainty of the Nusselt number at Re $= 6 \times 10^4$. (**a**) Target surface. (**b**) Impingement surface.

3. Results and Discussion

3.1. Two-Dimensional Distributions of Nusselt Numbers

The two-dimensional distributions of the Nusselt number on the target surface at different impingement Reynolds numbers are shown in Figure 7. Several spots can be found on the contours of the Nusselt number, as the temperature cannot be converted by the hue. However, it does not affect the analysis of the heat transfer. The impingement-enhanced heat transfer region is mainly located between the second and fourth rows of pin fins next to the impingement holes. The Nusselt numbers in the stagnation region are significantly high. The value at the stagnation point corresponding to the middle impingement hole is the largest, while the value at the stagnation point corresponding to the other two impingement holes is smaller, which may be because the jet flow from the two holes is affected by the side walls. The second peak values are found at all Reynolds numbers studied for a short distance of the target surface to the impingement surface. This phenomenon becomes significant with the further increase of the Reynolds number. This means a short jet impingement distance can improve the heat transfer rate on the target surface. The coolant easily flows to the film hole through the midspan region of the neighboring pin fins next to the stagnation region, resulting in somewhat high Nusselt number in this region. The bleeding of the coolant also leads to a weak enhancement of the heat transfer near the film holes. The Nusselt numbers decrease by 80–90% from the second peak to the film hole row. With the increase of the Reynolds number, the high heat transfer area expands, and the Nusselt number on the corresponding region is also increased. The difference of the Nusselt number at the second peak and the stagnation point decreases with the increasing Reynolds number.

The distributions of the Nusselt number on the impingement surfaces are different from those on the target surface, as shown in Figure 8. There are two regions with high Nusselt numbers at the left and right sides of the pin fins in the same row as the impingement holes. After the impingement, some of the coolant from the two adjacent impingement holes sinks in this region, resulting in the high turbulence intensity and the high heat transfer level. The regions next to the leading edges of the pin fins have higher heat transfer coefficients compared with the region near the trailing edges. The area with high Nusselt numbers enlarges with the increase of the Reynolds number.

The two-dimensional distributions of the Nusselt numbers on the pin fins A, B and C at the Reynolds number of 3×10^4 are shown in Figures 9–11. Since the structure of the test configuration is symmetrical, the heat transfer distributions of pin fins D and E are not measured. Some area of the pin fin is not visible when shooting normally to the axis of the pin fin, so the camera shoot slants the pin fin from the target wall. The pin fin A is the farthest from the impingement hole, and the wall jet becomes very weak. The distributions of the Nusselt number in the direction of the pin fin height are relatively uniform due to the relatively uniform velocity. The Nusselt numbers of pin fin B are

significantly larger than those of pin fin A. The Nusselt numbers in the region next to the target surface are relatively larger, rising to a peak value of 167 on the leading edge. Pin fin C is in the same row with the impingement hole. The heat transfer increases further, and the larger high Nusselt number region can be found on the leading region near the top of the pin fin. The reason for this is that the region is subjected to the high velocity crossflow transformed from the coolant jet.
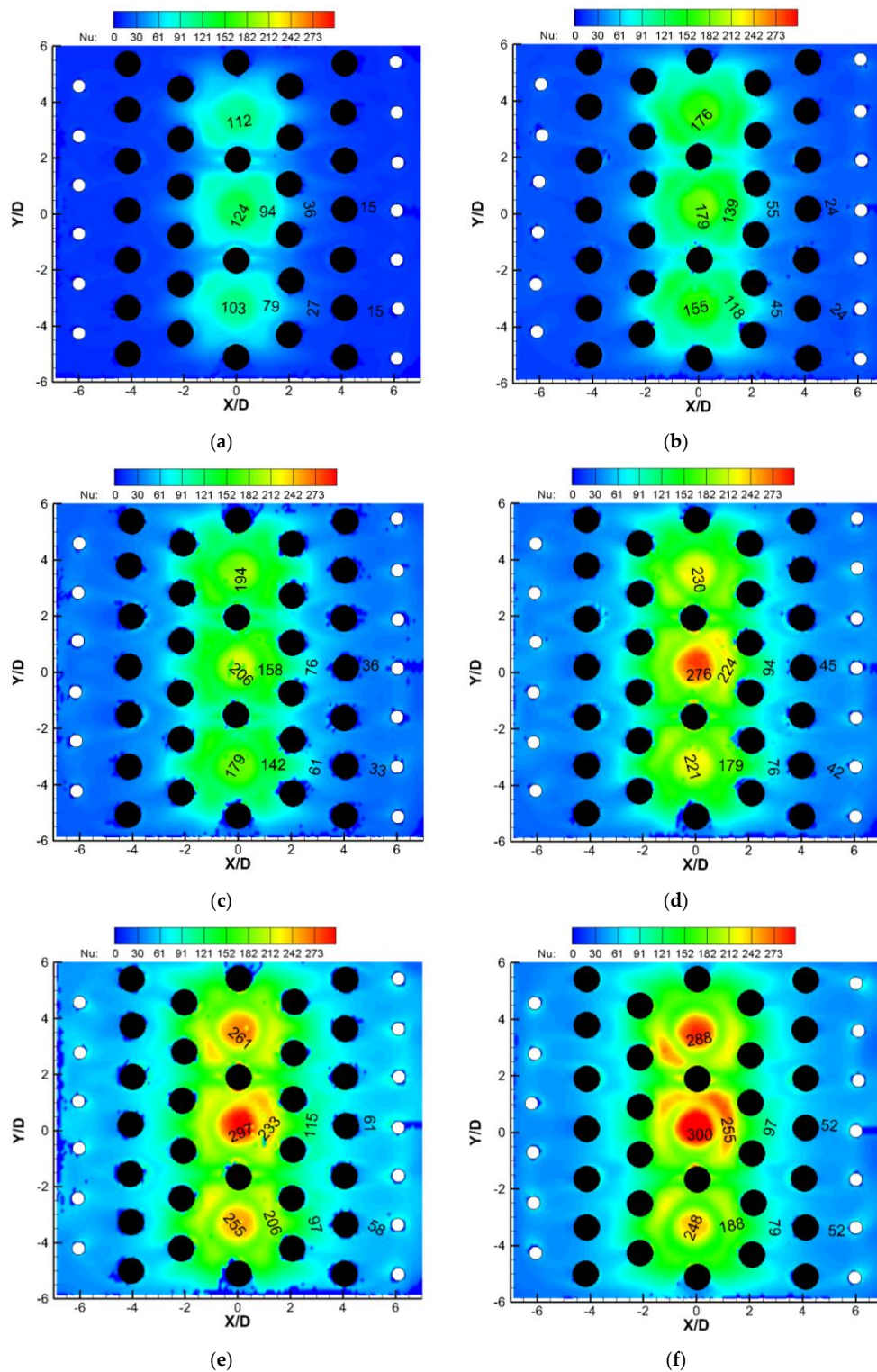
Figure 7. Two-dimensional distributions of the Nusselt number on the target surface. (**a**) Re = 1×10^4, (**b**) Re = 2×10^4, (**c**) Re = 3×10^4, (**d**) Re = 4×10^4, (**e**) Re = 5×10^4 and (**f**) Re = 6×10^4.
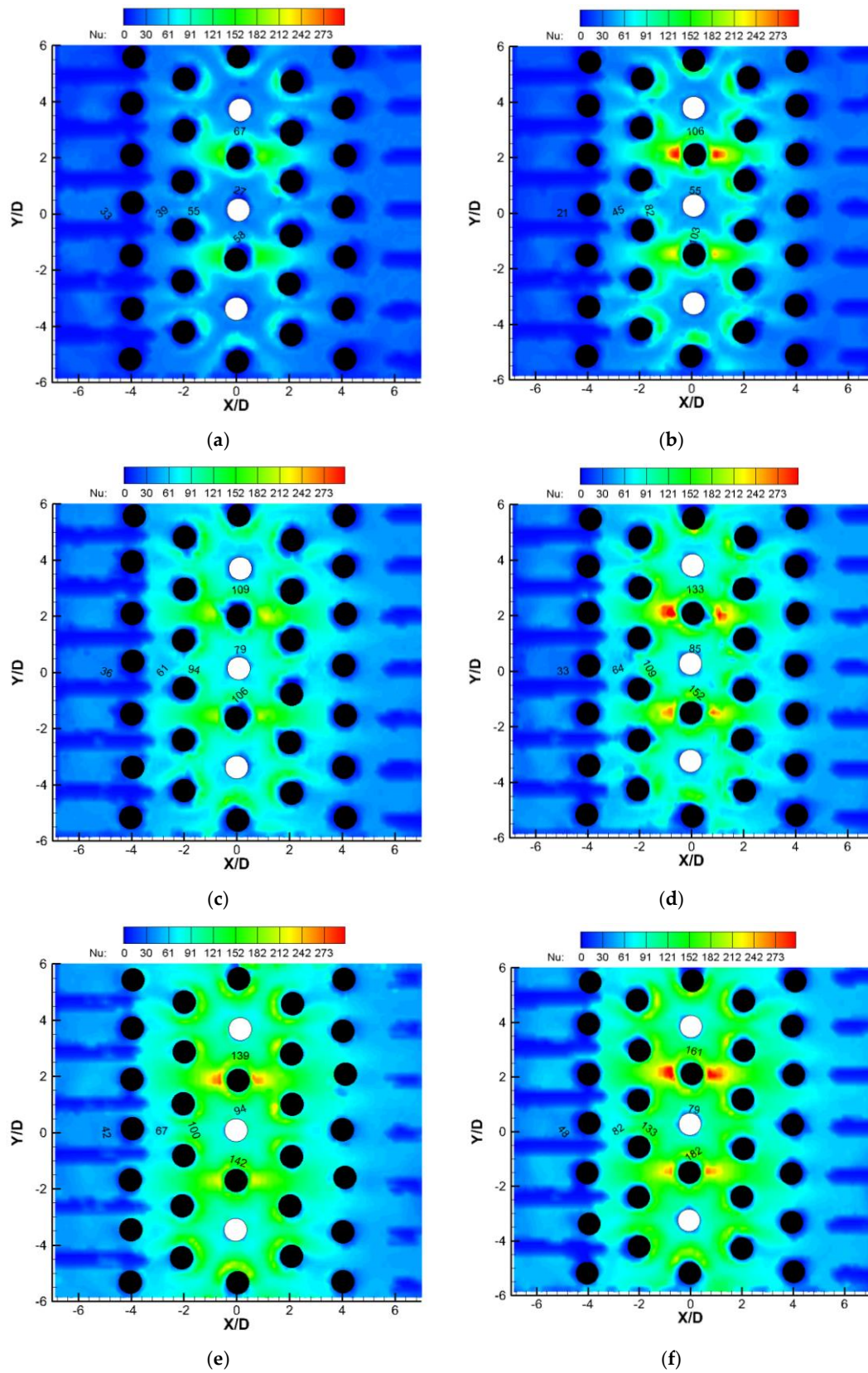
Figure 8. Two-dimensional distributions of the Nusselt number on the impingement surface. (**a**) Re = 1×10^4, (**b**) Re = 2×10^4, (**c**) Re = 3×10^4, (**d**) Re = 4×10^4, (**e**) Re = 5×10^4 and (**f**) Re = 6×10^4.
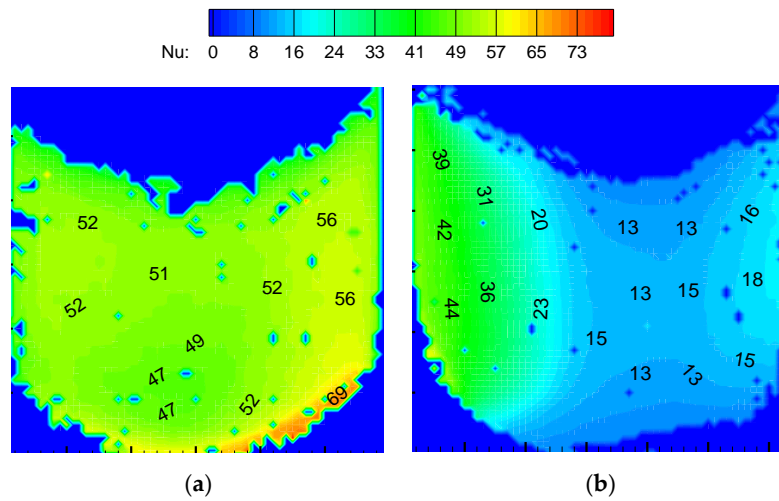
Figure 9. Nusselt number distributions on the pin fin A surface at Re = 3×10^4. (**a**) View angle 1. (**b**) View angle 2.
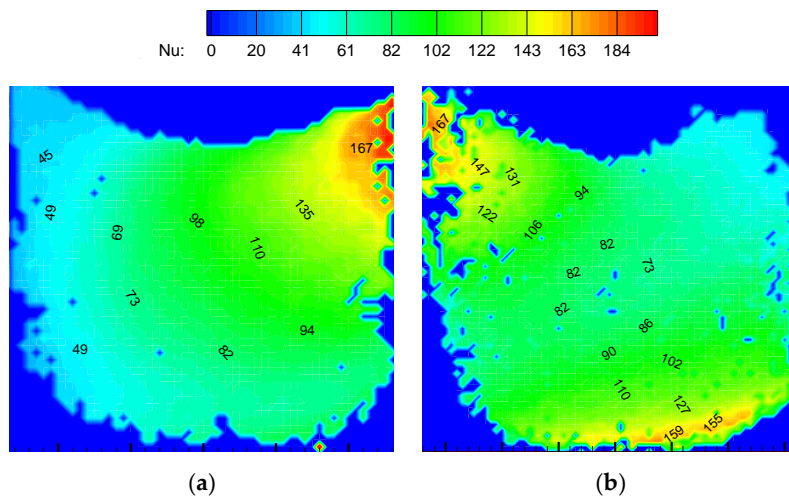
Figure 10. Nusselt number distributions on the pin fin B surface at Re = 3×10^4. (**a**) View angle 1. (**b**) View angle 2.
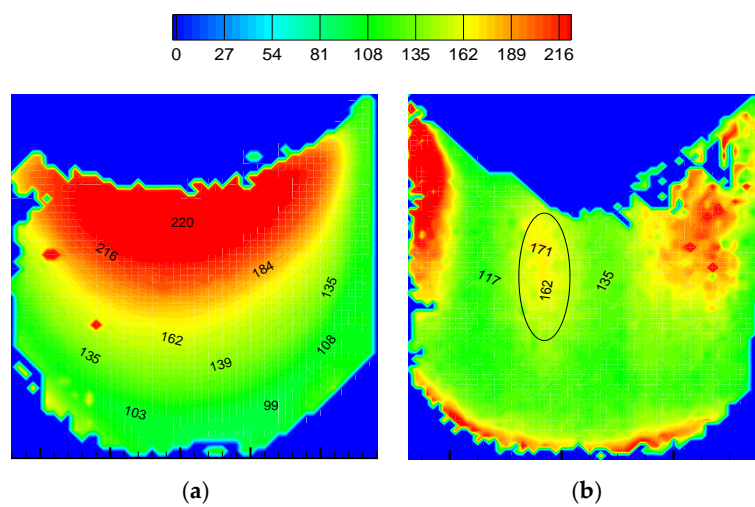
Figure 11. Nusselt number distributions on the pin fin C surface at Re = 3×10^4. (**a**) View angle 1. (**b**) View angle 2.

3.2. Spanwise Averaged Nusselt Numbers

The spanwise averaged Nusselt numbers on the target surface and impingement surface are plotted in Figure 12. The location of X/D = 0 is the center of the impingement hole. All the curves of the target surface show the same trends, decreasing with an increase of the absolute value of X/D between −5 to 5. Then, the curves slightly go upward due to the bleeding of the coolant from the film holes. The curves have much higher slopes at X/D in the range from −3 to 3 than those from −6 to −3 and from 3 to 6. The increase of the Reynolds number strengthens the heat transfer on the target surface. The spanwise averaged Nusselt numbers on the impingement surface decrease with the increase of the distance from the impingement point, except for X/D = 0 and −4. The higher the Reynolds number, the steeper the slope of the curve.

(**a**)　　　　　　　　　　　　　　　　　　　　　　　　(**b**)
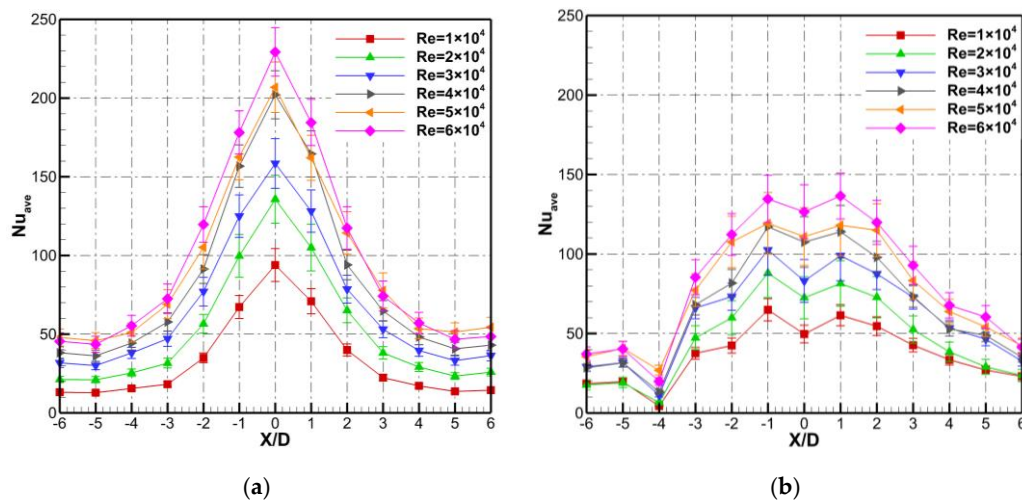
Figure 12. Spanwise averaged Nusselt number. (**a**) Target plate. (**b**) Impingement plate.

3.3. Surface-Averaged Nusselt Numbers

Figure 13 shows the surface averaged Nusselt numbers on the target surface, impingement surface and pin fin surfaces. The surface averaged Nusselt numbers on the target and impingement surfaces are nearly the same at the Reynolds number of 1×10^4. This implies that the heat transfer enhancement caused by the impingement was very weak at a small Reynolds number. When the Reynolds number is greater than 1×10^4, the values on the target surface are larger than those on the impingement surface. This effect becomes significant with the increase of the Reynolds number. The averaged value on the target surface is 23% larger than that on the impingement surface when the Reynolds number reaches 6×10^4. The surface averaged Nusselt numbers of pin fins A, B and C versus the Reynolds number vary greatly. The pin fins C and A have the shortest and longest distances from the stagnation point, resulting in the largest and the smallest Nusselt numbers, respectively. The Nusselt numbers of pin fins B and C are 130% and 570% larger than those of pin fin A at the small Reynolds number of 1×10^4, and the corresponding values are 56% and 127% at the large Reynolds number of 6×10^4. The correlations for the target surface, impingement surface and various pin fins are developed for the Nusselt number as a function of the Reynolds number, according to the experimental data, as follows:

Target surface:

$$Nu_{ave\_s} = 0.1148 \text{Re}^{0.6176}, \ 10,000 \le \text{Re} \le 60,000 \tag{7}$$

Impingement surface:

$$Nu_{ave\_s} = 0.5118 \text{Re}^{0.4614}, \ 10,000 \le \text{Re} \le 60,000 \tag{8}$$

Pin fin A:

$$Nu_{ave\_s} = 0.1125 \text{Re}^{0.7564}, \ 10,000 \le \text{Re} \le 60,000 \tag{9}$$

Pin fin B:

$$Nu_{ave\_s} = 0.2674\text{Re}^{0.5584}, \ 10,000 \le \text{Re} \le 60,000 \tag{10}$$

Pin fin C:

$$Nu_{ave\_s} = 23.3358\text{Re}^{0.1876}, \ 10,000 \le \text{Re} \le 60,000 \tag{11}$$

The results calculated by the correlations agree well with the experimental data. These corrections can be used to guide the heat transfer analysis.
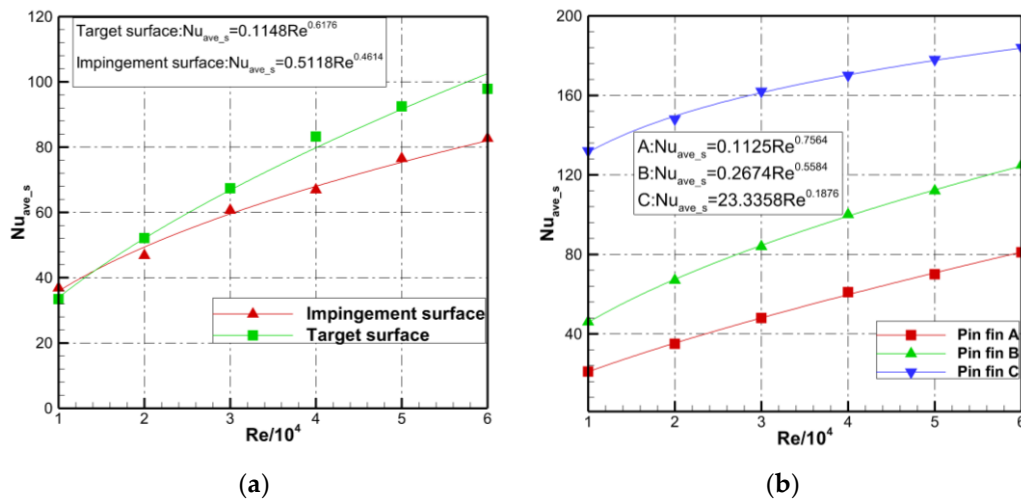
Figure 13. Surface-averaged Nusselt number. (**a**) Target surface and impingement surface. (**b**) Pin fin surface.

3.4. Heat Transfer Analysis of the Double-Wall Cooling Structure

Although the internal surfaces of the double-wall structure have high heat transfer coefficients and a significantly expanded heat transfer area, the wall temperature is gradually reduced in the process of the heat transfer from the target surface to the pin fin surface and the impingement surface. The different temperatures, areas and heat transfer coefficients on the surfaces result in the different contributions to the overall heat transfer enhancement. The heat load, transferred from the gas to the double-wall through the target plate, is partly transported to the coolant through the target surface, and then, the rest is transferred by heat conduction to the pin fins and impingement plate, at which it is finally transmitted to the coolant by convection heat transfer. The individual contribution of the pin fin surface, impingement surface and target surface to the overall heat transfer rate are analyzed as follows.

The Nusselt numbers on pin fins A, B and C are considered as the averaged values of the pin fins in the same row. The pin fins, target surface and impingement surfaces are divided into five regions to obtain the average heat transfer coefficients, as shown in Figure 14. Subtracting the circular areas of the pin fins and the impingement hole from the corresponding five regions on the impingement surface, the remaining area divided by the number of the pin fins in each region is considered as the additional lateral area A_r of the pin fin. The additional heights H'_{Pf} of the pin fins, as shown in Figure 15, can be obtained by Equation (12), resulting in the equivalent heights H of the pin fins calculated by Equation (13).

$$H'_{Pf} = \frac{A_r}{\pi D_{Pf}} \tag{12}$$

$$H = H_{Pf} + H'_{Pf} \tag{13}$$
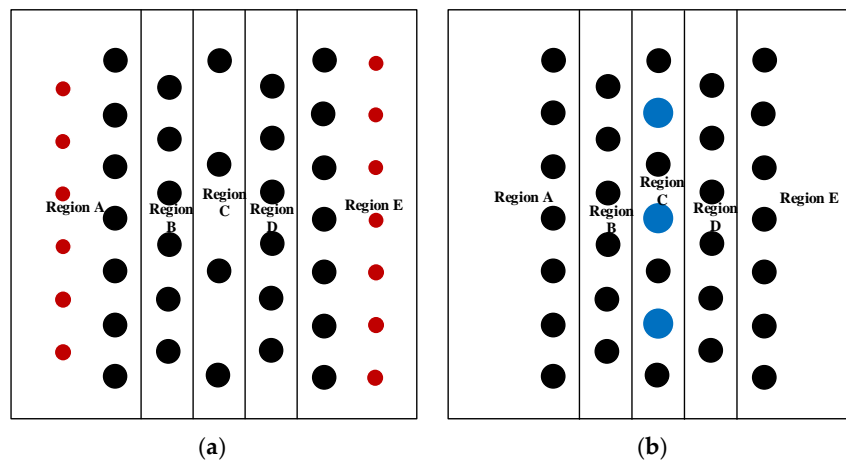
Figure 14. Regions on the surfaces. (**a**) Target surface. (**b**) Impingement surface.
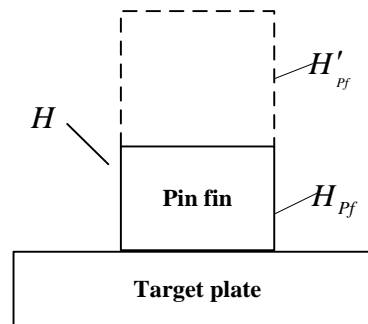
Figure 15. Height of the pin fin.

The equivalent heat transfer coefficients on the pin fins are represented by Equations (14)–(16).

$$h_A = h_{\text{Pf–A}} \frac{H_{Pf-A}}{H} + h_{\text{Ip–A}} \frac{H'_{Pf-A}}{H} \tag{14}$$

$$h_B = h_{\text{Pf–B}} \frac{H_{Pf-B}}{H} + h_{\text{Ip–B}} \frac{H'_{Pf-B}}{H} \tag{15}$$

$$h_C = h_{\text{Pf–C}} \frac{H_{Pf-C}}{H} + h_{\text{Ip–C}} \frac{H'_{Pf-C}}{H} \tag{16}$$

The solid thermal conductivity λ_{solid} of 20 W/(m × K) is considered. This is a typical thermal conductivity value of the blade material in the engine operating temperature. The efficiency of the pin fin is calculated by Equation (17) [35]. The efficiencies of the equivalent pin fin with additional height are designated as η_A, η_B and η_C, which are also computed by Equation (17) using the equivalent heights and equivalent heat transfer coefficients:

$$\eta = \frac{\tan h(mH)}{mH} \tag{17}$$

where $m = \sqrt{\frac{4h}{\lambda_{solid} D_{pf}}}$.

The heat transfer rate of the target surface and pin fins are calculated by Equations (18) and (19):

$$\Phi_{Tp} = \sum h_{\text{Tp}} \times A_{Tp} \times (t - t_f) = (h_{\text{Tp–A}} \times A_{Tp-A} + h_{\text{Tp–B}} \times A_{Tp-B} + h_{\text{Tp–C}} \times A_{Tp-C} + h_{\text{Tp–D}} \times A_{Tp-D} + h_{\text{Tp–E}} \times A_{Tp-E}) \times (t - t_f) \tag{18}$$

$$\Phi_{Pf} = (2 \times \eta_{Pf-A} \times h_{Pf-A} \times A_{Pf-A} + 2 \times \eta_{Pf-B} \times h_{Pf-B} \times A_{Pf-B} + \eta_{Pf-C} \times h_{Pf-C} \times A_{Pf-C}) \times (t - t_f) \tag{19}$$

Here, $A_{Tp-A}, A_{Tp-B}, A_{Tp-C} A_{Tp-D}$ and A_{Tp-E} are the areas on the target plate in regions A, B, C and D subtracting the circular areas of the pin fins or film holes in the corresponding regions.

The total heat transfer rate on the impingement and pin fin surfaces is calculated by Equation (20):

$$\Phi' = (2 \times \eta_A \times h_A \times \pi \times D_{Pf} \times H_A + 2 \times \eta_B \times h_B \times \pi \times D_{Pf} \times H_B + \eta_C \times h_C \times \pi \times D_{Pf} \times H_C) \times (t - t_f) \quad (20)$$

By subtracting the heat transfer rate of the pin fin surfaces Φ_{Pf} from the total value Φ', the heat transfer rate of the impingement surface Φ_{Ip} is obtained from Equation (21):

$$\Phi_{Ip} = \Phi' - \Phi_{Pf} \quad (21)$$

Finally, the total heat transfer rate on the internal surfaces is computed by Equation (22):

$$\Phi_{is} = \Phi_{Tp} + \Phi_{Pf} + \Phi_{Ip} \quad (22)$$

The percentages of the heat transfer rate on the pin fin surface, impingement surface and target surface to the whole internal heat transfer rate are defined as $\Phi_{Pf}/\Phi_{is}, \Phi_{Ip}/\Phi_{is}$ and Φ_{Tp}/Φ_{is}, as shown in Figure 16. These results reveal that the target surface contributes the largest amount of heat transfer rate, with a value of about 62%. The contribution of the impingement surface is from 18% to 21%, which is slightly larger than that of the pin fin surfaces from 16% to 18%. Additionally, the two curves tend to be the same as the Reynolds number increases.
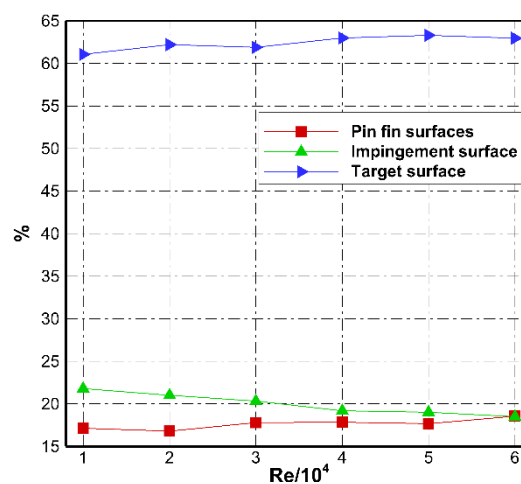
Figure 16. Percentage of the heat transfer rate on the surfaces.

4. Conclusions

The heat transfer coefficients on the internal impingement surface, target surface and pin fin surfaces of a double-wall structure were measured by the TLC technique. The corrections of the Nusselt numbers were developed as a function of the Reynolds number. The heat transfer process of the internal surfaces of the double-wall structure was analyzed in detail. The main findings are as follows:

1. For the target surface, the high heat transfer area is mainly between the two rows of pin fins next to the impingement holes. The second peak values are found at all Reynolds numbers studied in this paper. With the increase of the Reynolds number, the difference between the Nusselt number at the second peak and the stagnation point decreases. It means a short jet impingement distance can improve the heat transfer rate on the target surface. For the impingement surface, the regions with the highest Nusselt numbers appear at the left and right sides of the pin fins between the two impingement holes. The averaged Nusselt numbers on the target surface are 0–23% larger

than those on the impingement surface, with the increase of the Reynolds number from 1×10^4 to 6×10^4.

2. The Nusselt numbers on the pin fins are strongly dependent on the various locations. Pin fin C has a much higher surface-averaged Nusselt number than that of pin fin B and pin fin A, which has the smallest value. The correlations for the various pin fins, target surface and impingement surface are developed to guide the heat transfer analysis.

3. The heat transfer contributions of the impingement surface, pin fin surface and target surface to the overall cooling are analyzed. The target surface contributed the largest amount of the heat transfer rate, with a value of about 62%. The percentage of the heat transfer contribution is from 18% to 21% for the impingement surface and increases from 16% to 18% for the pin fin surfaces within the studied Reynolds numbers. The total heat transfer contribution of the impingement surface and pin fin surface is 38%, which should be carefully studied for the accurate design of the gas turbine blade-cooling technique.

Conflicts of Interest: The authors declare no conflict of interest.

Nomenclature

X	streamwise direction of test rig
Y	spanwise direction of test rig
L	the distance between the film hole and the adjacent pin-fin in X direction (m)
P	film hole spacing in the Y direction (m)
S	the distance between the pin-fins (m)
V	averaged velocity magnitude of coolant at the impingement hole inlet (m/s)
T	Kelvin temperature (K)
t	Celsius temperature (°C)
D	diameter of impingement hole (m)
A	area (m^2)
H	Height (m)
Φ	heat transfer rate (W)

Greek Letters

ρ	density (kg/m^3)
λ	thermal conductivity (W/(m×K))
μ	dynamic viscosity (kg/(m×s))
n	the number of the spanwise pixels at the fixed x coordination
m	the number of the streamwise pixels at the fixed y coordination
τ	the color change time of the liquid crystal coating (s)
i	time step
η	fin efficiency

Subscripts

I	impingement
w	wall
k	serial number of the pixels in streamwise
j	serial number of the pixels in spanwise

ave	spanwise averaged
ave-s	surface averaged
cir	circumferential
c	coolant
o	initial time
Ip	impingement plate
Pf	pin fin
Tp	target plate
Is	internal surface

References

1. Alenezi, A.H.; Almutairi, A.; Alhajeri, H.M.; Addali, A.; Gamil, A.A.A. Flow structure and heat transfer of jet impingement on a rib-roughened flat plate. *Energies* **2018**, *11*, 1550. [CrossRef]

2. Faris Abdullah, M.; Zulkifli, R.; Harun, Z.; Abdullah, S.; Wan Ghopa, W.A. Experimental and numerical simulation of the heat transfer enhancement on the twin impingement jet mechanism. *Energies* **2018**, *11*, 927. [CrossRef]

3. Taslim, M.E.; Bethka, D. Experimental and numerical impingement heat transfer in an airfoil leading-edge cooling channel with cross-flow. *J. Turbomach.* **2009**, *131*, 011021. [CrossRef]

4. Liu, L.L.; Zhu, X.C.; Liu, H.; Du, Z.H. Effect of tangential jet impingement on blade leading edge impingement heat transfer. *Appl. Therm. Eng.* **2018**, *130*, 1380–1390. [CrossRef]

5. Shashikant, P.; Kumar, P.D. The Impingement Heat Transfer Data of Inclined Jet in Cooling Applications: A Review. *J. Therm. Sci.* **2020**, *29*, 11–12.

6. Fu, J.L.; Cao, Y.; Zhang, C.; Zhu, J.Q. Investigation of the Conjugate Heat Transfer and Flow Field for a Flat Plate with Combined Film and Impingement Cooling. *J. Therm. Sci.* **2020**, *29*, 955–971. [CrossRef]

7. Li, G.C.; Yang, P.; Zhang, W.; Wu, Z.; Kou, Z.H. Enhanced film cooling performance of a row of cylindrical holes embedded in the saw tooth slot. *Int. J. Heat Mass Tran.* **2019**, *132*, 1137–1151. [CrossRef]

8. Fu, W.S.; Chao, W.S.; Tsubokura, M.; Li, C.G.; Wang, W.H. Direct numerical simulation of film cooling with a fan-shaped hole under low Reynolds number conditions. *Int. J. Heat Mass Tran.* **2018**, *123*, 544–560. [CrossRef]

9. Ries, F.; Li, Y.X.; Klingenberg, D.; Nishad, K.; Janicka, J.; Sadiki, A. Near-wall thermal processes in an inclined impinging jet: analysis of heat transport and entropy generation mechanisms. *Energies* **2018**, *11*, 1354. [CrossRef]

10. Carol, E.B.; Connor, J.W.; James, L.R.; Marc, D.P. Experimental evaluations of the relative contributions to overall effectiveness in turbine blade leading edge cooling. *J. Turbomach.* **2019**, *141*, 041007.

11. Kyle, C.; Thomas, N.S.; David, B. Experimentally measured effects of incidence angle on the adiabatic and overall effectiveness of a fully cooled turbine airfoil with shaped showerhead holes. *J. Turbomach.* **2017**, *139*, 091007.

12. Mensch, A.; Thole, K.A. Overall Effectiveness of a blade endwall with jet impingement and film cooling. *J. Eng. Gas Turb. Power.* **2014**, *136*, 031901. [CrossRef]

13. Williams, R.P.; Dyson, T.E.; Bogard, D.G.; Bradshaw, S.D. Sensitivity of the overall effectiveness to film cooling and internal cooling on a turbine vane suction side. *J. Turbomach.* **2014**, *136*, 031006. [CrossRef]

14. Moreno, G.; Narumanchi, S.; Venson, T.; Bennion, K. Micro structured surfaces for single-phase jet impingement heat transfer enhancement. *J. Sci. Eng. App.* **2013**, *5*, 031004.

15. Singh, P.; Zhang, M.Y.; Ahmed, S.; Ramakrishnan, K.R.; Ekkad, S. Effect of micro-roughness shapes on jet impingement heat transfer and fin-effectiveness. *Int. J. Heat Mass Tran.* **2019**, *132*, 80–95. [CrossRef]

16. Rao, Y.; Chen, P.; Zhu, J.Q. An Experimental Study of Impingement Heat Transfer on the Surfaces with Micro W-Shaped Ribs. In Proceedings of the ASME Turbo Expo, Montreal, Canada, 15–19 June 2015. GT2015.

17. Vinze, R.; Khade, A.; Kuntikana, P.; Ravitej, M.; Suresh, B.; Kesavan, V.; Prabhu, S.V. Effect of dimple pitch and depth on jet impingement heat transfer over dimpled surface impinged by multiple jets. *Int. J. Sci.* **2019**, *145*, 105974. [CrossRef]

18. Andrews, G.E.; Hussain, R.A.; Mkpadi, M.C. Enhanced impingement heat transfer: The influence of impingement X/D for interrupted rib obstacles (rectangular pin fins). *J. Turbomach.* **2006**, *128*, 321–330. [CrossRef]

19. Wang, L.; Sundén, B.; Borg, A.; Abrahamsson, H. Control of jet impingement heat transfer in crossflow by using a rib. *Int. J. Heat Mass Tran.* **2011**, *54*, 4157–4166. [CrossRef]

20. Isman, M.K.; Can, M. Experimental investigation of impingement heat transfer from a round rib-roughened surface. *Heat Mass Transf.* **2017**, *53*, 1405–1412. [CrossRef]

21. Xu, Y.; Zhu, H.R.; Xu, W.J.; Liu, C.L. Effect of pin fin arrangement on the heat transfer characteristics in a convergent channel with impingement. *Int. J. Heat Mass Transf.* **2018**, *125*, 629–639. [CrossRef]

22. Rao, Y.; Liu, Y.Y.; Wan, C.Y. Multiple-jet impingement heat transfer in double-wall cooling structures with pin fins and effusion holes. *Int. J. Sci.* **2018**, *133*, 106–119. [CrossRef]

23. Liu, Y.H.; Song, S.J.; Lo, Y.H. Jet impingement heat transfer on target surfaces with longitudinal and transverse grooves. *Int. J. Heat Mass Tran.* **2013**, *58*, 292–299. [CrossRef]

24. Wang, C.L.; Wang, L.; Sundén, B. A novel control of jet impingement heat transfer in cross-flow by a vortex generator pair. *Int. J. Heat Mass Tran.* **2015**, *88*, 82–90. [CrossRef]

25. Singh, D.; Premachandran, B.; Kohli, S. Effect of nozzle shape on jet impingement heat transfer from a circular cylinder. *Int. J. Sci.* **2015**, *96*, 45–69. [CrossRef]

26. Bu, X.Q.; Peng, L.; Lin, G.P.; Bai, L.Z.; Wen, D.S. Experimental study of jet impingement heat transfer on a variable-curvature concave surface in a wing leading edge. *Int. J. Heat Mass Tran.* **2015**, *90*, 92–101. [CrossRef]

27. Pachpute, S.; Premachandran, B. Effect of number of round jets on impingement heat transfer from a heated Cylinder. *App. Eng.* **2019**, *162*, 114308. [CrossRef]

28. Ansu, U.; Godi, S.C.; Pattamatta, A.; Balaji, C. Experimental investigation of the inlet condition on jet impingement heat transfer using liquid crystal thermography. *Exp. Fluid Sci.* **2017**, *80*, 363–375. [CrossRef]

29. Chen, L.L.; Brakmann, R.G.A.; Weigand, B.; Crawford, M.; Poser, R. Detailed heat transfer investigation of an impingement jet array with large jet-to-jet distance. *Int. J. Sci.* **2019**, *146*, 106058. [CrossRef]

30. Schulz, S.; Brack, S.; Terzis, A. On the effects of coating thickness in transient heat transfer experiments using thermochromic liquid crystals. *Exp. Fluid Sci.* **2016**, *70*, 196–207. [CrossRef]

31. Satta, F.; Tanda, G. Measurement of local heat transfer coefficient on the endwall of a turbine blade cascade by liquid crystal thermography. *Exp. Fluid Sci.* **2014**, *58*, 209–215. [CrossRef]

32. Zhou, D.W.; Sun, C.; Liu, L.L.; Zhu, X.C.; Du, Z.H. The effect and correction of concave surfaces on heat transfer in the transient TLC technique. *App. Eng.* **2019**, *150*, 412–420. [CrossRef]

33. Abernethy, R.B.; Benedict, R.P.; Dowdell, R.B. ASME measurement uncertainty. *J. Fluids Eng.* **1985**, *107*, 161–164. [CrossRef]

34. Vedula, R.P.; Metzger, D.E.; Bickford, W.B. Effects of Lateral and Anisotropic Conduction on Determination of Local Convection Heat Transfer Characteristics with Transient Tests and Surface Coatings. In Proceedings of the ASME Winter Annual Meeting, Chicago, IL, USA, 27 November–2 December 1988; pp. 21–27.

35. Bergman, T.L.; Incropera, F.P.; DeWitt, D.P.; Lavine, A.S. *Fundamentals of Heat and Mass Transfer*, 7th ed.; John Wiley &Sons, Inc.: New York, NY, USA, 2007; pp. 164–166.